

# Multi-scale analysis of global electromagnetic instabilities in ITER Pre-Fusion-Power Operation plasmas

**T. Hayward-Schneider<sup>1</sup>, Ph. Lauber<sup>1</sup>, A. Bottino<sup>1</sup>,  
A. Mishchenko<sup>2</sup>**

<sup>1</sup> Max-Planck-Institut für Plasmaphysik, Boltzmannstr. 2, 85748 Garching, Germany

<sup>2</sup> Max-Planck-Institut für Plasmaphysik, Wendelsteinstr. 1, 17491 Greifswald, Germany

E-mail: [thomas.hayward@ipp.mpg.de](mailto:thomas.hayward@ipp.mpg.de)

Global electromagnetic gyrokinetic simulations are performed with the Particle-in-Cell code ORB5 for an ITER Pre-Fusion-Power-Operation (PFPO) plasma scenario, with half-field (2.65 T) and half-current (7.5 MA). We report on a ‘multi-scale’ analysis of the discharge, considering eigenmodes and instabilities across three scale-lengths. Although the scenario will nominally have neutral beam heating with particles injected with 1 MeV, Alfvén eigenmodes are investigated in the absence of such source, and Reversed Shear (RSAE), Toroidal (TAE) and Elliptical (EAE) Alfvén eigenmodes are found with weak damping for moderately low toroidal mode numbers ( $10 < n < 35$ ). At higher toroidal mode numbers ( $40 \leq n \leq 70$ ), unstable Alfvénic modes have been observed close to rational surfaces and are labelled as Beta-induced Alfvén eigenmodes (BAE)/Alfvénic Ion Temperature Gradient (AITG) modes, since their frequency is associated with the BAE gap and they are driven by the bulk plasma on the Alfvénic continuum. These modes are unstable in the absence of energetic particles, and adding a species of energetic particles (with an isotropic 1 MeV slowing down distribution) has negligible impact on their growth rate. At higher toroidal mode numbers ( $150 \lesssim n < 220$ ), low frequency microscale instabilities are observed.

## 1. Introduction

Energetic particles (EPs), such as Neutral Beam Injection (NBI) or alpha particles generated by fusion reactions, can have a significant impact on the stability of electromagnetic instabilities in tokamak plasmas. In turn, these instabilities can lead to energetic particle transport, or losses, affecting the efficiency of the plasma heating, or potentially increasing wall heat loads. In addition, the bulk plasma can also interact with these electromagnetic instabilities, not only contributing to the damping, but in some cases also driving these instabilities.

In previous work, we studied the effect of alpha particle drive on Alfvén eigenmodes in a  $Q = 10$  scenario for ITER. In this paper, we consider a broad range of electromagnetic instabilities potentially present in the pre-fusion-power-operation (PFPO) phase of ITER. Specifically, we consider a scenario with a half-field, half-current, hydrogen plasma, and 1 MeV neutral beam injection (NBI). We consider the Alfvén eigenmodes which may potentially be destabilized by the NBI ions, and also smaller scale instabilities, namely meso-scale Alfvénic modes such as Beta-induced Alfvén eigenmodes/Alfvénic Ion Temperature Gradient modes (BAE/AITG), as well as microscale instabilities such as those associated with (electromagnetic) turbulence.

In this work, we use the global electromagnetic gyrokinetic particle-in-cell code ORB5 [1, 2] for the simulations, which are also compared to Alfvén continuum calculations using the linear global gyrokinetic eigenvalue solver LIGKA [3].

This paper is organized as follows: §2 describes the theoretical model used for the calculations, and the numerical implementation of the numerical tool ORB5; §3 outlines the scenario being studied in this work; §4 presents the results, split into three sections: linear Alfvén eigenmodes which might be driven unstable by EPs, unstable AEs driven by the bulk plasma, and instabilities associated with microturbulence. Finally, §5 presents a summary and outlook of the paper.

## 2. Physical model

In this work, the numerical results presented are obtained using the ORB5 code [1]. This is a global electromagnetic gyrokinetic particle-in-cell (PIC) code which uses markers to sample the 5D phase space

$(\mathbf{R}, v_{\parallel}, \mu)$ , with the equations independent of the gyrophase, and the magnetic moment ( $\mu$ ) of a marker constant in the absence of collisions.

The perturbed part of the distribution function is then evolved according to the gyrokinetic Vlasov equation

$$\frac{d}{dt} \delta f_s = -\dot{\mathbf{R}} \cdot \frac{\partial F_{0s}}{\partial \mathbf{R}} \Big|_{\epsilon, \mu} - \dot{\epsilon} \cdot \frac{\partial F_{0s}}{\partial \epsilon} \Big|_{\mathbf{R}, \mu} \quad (1)$$

(where subscript  $s$  denotes a plasma species  $s$ ) according to the equations for the particle equations of motion

$$\begin{aligned} \dot{\mathbf{R}} = & v_{\parallel} \mathbf{b} - v_{\parallel}^2 \frac{cm_s}{qB_{\parallel}^*} \mathbf{G} + \mu \frac{Bcm_s}{qB_{\parallel}^*} \mathbf{b} \times \frac{\nabla B}{B} + \\ & \frac{\mathbf{b}}{B_{\parallel}^*} \times \nabla \langle \phi - v_{\parallel} A_{\parallel}^s - v_{\parallel} A_{\parallel}^h \rangle - \frac{q_s}{m_s} \langle A_{\parallel}^h \rangle \mathbf{b}^* \end{aligned} \quad (2)$$

$$\begin{aligned} \dot{v}_{\parallel} = & \mu B \nabla \cdot \mathbf{b} + \mu v_{\parallel} \frac{cm_s}{q_s B_{\parallel}^*} \mathbf{G} \cdot \nabla B - \mu \frac{\mathbf{b} \times \nabla B}{B_{\parallel}^*} \cdot \nabla \langle A_{\parallel}^{(s)} \rangle \\ & - \frac{q_s}{m_s} \left[ \mathbf{b}^* \cdot \nabla \langle \phi - v_{\parallel} A_{\parallel}^{(h)} \rangle + \frac{\partial}{\partial t} \langle A_{\parallel}^{(s)} \rangle \right] \end{aligned} \quad (3)$$

$$\dot{\epsilon} = v_{\parallel} \dot{v}_{\parallel} + \mu \nabla B \cdot \dot{\mathbf{R}} \quad (4)$$

where  $\mathbf{B} = \nabla \times \mathbf{A}$ ,  $\mathbf{b} = \mathbf{B}/B$ ,  $B_{\parallel}^* = \mathbf{b} \times \mathbf{A}^*$

$$\mathbf{A}^* = \mathbf{A} + \left( \frac{m_s c}{q_s} v_{\parallel} + \langle A_{\parallel}^{(s)} \rangle \right) \mathbf{b}$$

$$\mathbf{b}^* = \frac{\nabla \times \mathbf{A}^*}{B_{\parallel}^*} = \mathbf{b} - \left( \frac{cm_s}{qB_{\parallel}^*} v_{\parallel} + \langle A_{\parallel}^{(s)} \rangle \right) \mathbf{G}$$

$$\mathbf{G} = \mathbf{b} \times (\mathbf{b} \times (\nabla \times \mathbf{b}))$$

and with the gyroaveraged potential  $\langle \phi \rangle = \oint \phi(\mathbf{R} + \boldsymbol{\rho}) d\alpha / (2\pi)$  with  $\rho$  the gyroradius of the particle and  $\alpha$  the gyro-phase.

These equations are coupled to the field equations, the linearized gyrokinetic quasineutrality equation

$$-\nabla \cdot \left[ \left( \sum_s \frac{q_s^2 n_s c^2}{T_s} \rho_s^2 \right) \nabla_{\perp} \phi \right] = \sum_s q_s n_{1s} \quad (5)$$

For the parallel Ampère's law, the perturbed magnetic potential  $A_{\parallel}$  is split in to the symplectic part  $A_{\parallel}^{(s)}$ , which is found from

$$\frac{\partial}{\partial t} A_{\parallel}^{(s)} + \mathbf{b} \cdot \nabla \phi = 0 \quad (6)$$

and the Hamiltonian part  $A_{\parallel}^{(h)}$ , solved using the mixed-variable parallel Ampère's law,

$$\left( \sum_s \frac{\beta_s}{\rho_s^2} - \nabla_{\perp}^2 \right) A_{\parallel}^{(h)} = \mu_0 \sum_s j_{\parallel 1s} + \nabla_{\perp}^2 A_{\parallel}^{(s)} \quad (7)$$

with  $n_{1s} = \int d^6 Z \delta f_s \delta(\mathbf{R} + \boldsymbol{\rho} - \mathbf{x})$  the perturbed gyrocenter density,  $\rho_s = \sqrt{m_s T_s} / (q_s B)$  the thermal gyroradius,  $q_s$  the particle charge,  $d^6 Z = B_{\parallel}^* d\mathbf{R} dv_{\parallel} d\mu d\alpha$  the phase space volume,  $j_{1s} = \int d^6 Z v_{\parallel} \delta f_s \delta(\mathbf{R} + \boldsymbol{\rho} - \mathbf{x})$  the perturbed parallel gyrocenter current. Note that due to the scale separation between ion and electron Larmor radii, electrons are treated differently from ion species, and terms with  $\rho_e$  are neglected.

The particular method of using the mixed-variables formulation, and then applying a pullback procedure to the particles is described in reference [2], where its advantages for solving electromagnetic equations are discussed.

A set of straight field line coordinates are used, with radial coordinate  $s = \sqrt{\psi / \psi_{\text{edge}}}$  (where  $\psi$  is the poloidal flux), toroidal angle  $\varphi$ , and poloidal angle

$$\theta^* = \frac{1}{q(s)} \int_0^{\theta} \frac{\mathbf{B} \cdot \nabla \varphi}{\mathbf{B} \cdot \nabla \theta'} d\theta'$$

(where  $\theta$  is the geometric poloidal angle, and  $q(s)$  the safety factor) $\ddagger$ .

The field equations are solved on a basis of cubic finite elements and using Fourier methods in the two angular directions. This allows the use of Fourier filtering, which helps to reduce noise by excluding non-physical modes which are far from being field aligned [4]. The local poloidal Fourier filter will retain modes with poloidal mode numbers  $m_n(s) = [nq(s)] \pm \Delta m$  at each radial point for each toroidal mode  $n$ , where a typical values of  $\Delta m$  is 5.

The distribution function  $f(\mathbf{R}, v_{\parallel}, \mu, t)$  is separated into a time-independent background part ( $F_0(\Psi = s^2, E = \frac{1}{2}v_{\parallel}^2 + \mu B, v_{\parallel})$ ), and a time dependent part  $\delta f(\mathbf{R}, v_{\parallel}, \mu, t)$ . The time dependent part of the distribution function is represented by markers, using the so-called particle-in-cell (PIC) Lagrangian method, with each ‘‘marker’’ representing a small 5D volume of phase-space, and carrying a particle weight,  $w(t)$ . These markers are evolved using the equations of motion for the gyrocenters, and with a weight equation to evolve the weights. The fields are solved from the charge and current densities, calculated by depositing the charge/current from the markers using the gyrocenters for electron markers, and gyrings (using in this work a 4-point average) for the ion markers.

The system of particles and fields is evolved using a 4th-order Runge-Kutta timestepping scheme.

$\ddagger$   $\theta^*$  in ORB5 is often labelled elsewhere as  $\chi$ .

Linear simulations can be performed by linearizing equations for the particle trajectories and weights, equations 2, 3, and 4.

### 3. Scenario description

We consider a half-field, half-current ITER PFPO [5, 6] scenario, modelled using ASTRA [7] and made available at ITER through the Integrated Modelling & Analysis Suite (IMAS) [8]. The major radius,  $R = 6.2$  m; the minor radius,  $a = 2.0$  m; the magnetic field on axis  $B_0 = 2.65$  T; the bulk ions are H, with some additional Beryllium and Neon impurities ( $< 1\%$ ). The electron temperature profile is peaked, with the electron temperature on axis  $T_{e,s=0} \approx 8$  keV, and the electron temperature at the top of the pedestal ( $T_{e,\text{ped. top}} \approx 3$  keV). The main ion temperature profile has very similar core and pedestal top values, but the peaking profile is slightly different, with the steeper gradient region closer to the core than in the case of the electron temperature. Impurity ion species are taken to have the same temperature profiles as the main ion species. The density profiles of the ions and electrons (linked via quasineutrality and the impurity density profiles) are almost flat, but marginally peaked. The on-axis electron density  $n_{e,s=0} \approx 4 \times 10^{19} \text{ m}^{-3}$ . The temperature and density profiles for the background species are shown in figure 2(a).

These parameters give an Alfvén frequency ( $\omega_A$ ) on axis of  $1.58 \times 10^6 \text{ rad s}^{-1}$ , approximately  $\omega_{ci}/177$ .

The energetic particles in the scenario are from a negative-ion neutral beam injection (NBI, or N-NBI) source with a single birth energy of 1 MeV. In this work, when considered, the energetic particles, are modelled using an isotropic slowing down distribution [9] with birth energy 1 MeV. If we calculate the equivalent temperature by integrating moments of this distribution function, we find that this corresponds to 242 keV or  $T_{EP}/T_e = 30.9$  on axis, with the ratio decreasing to about 24 at the top of the pedestal. The profile of the equivalent temperature for the NBI is shown in figure 3. While this neglects the anisotropy present in a realistic distribution function (also considered in the ASTRA model), we leave an anisotropic analytical distribution function [10], or a numerical treatment of the NBI from ASTRA's Fokker-Plank solver to future work. In fact, we leave most of the modelling of drive from NBI ions to future work.

The profiles and equilibrium considered were taken from IMAS at ITER, the scenario in question being shot 101006, run 50. The equilibrium used was generated by running the CHEASE MHD equilibrium code [11] reading from IMAS, and outputting an file using the CHEASE-ORB5 interface.  $\S$

$\S$  CHEASE takes the equilibrium from IMAS/IDS as an input,

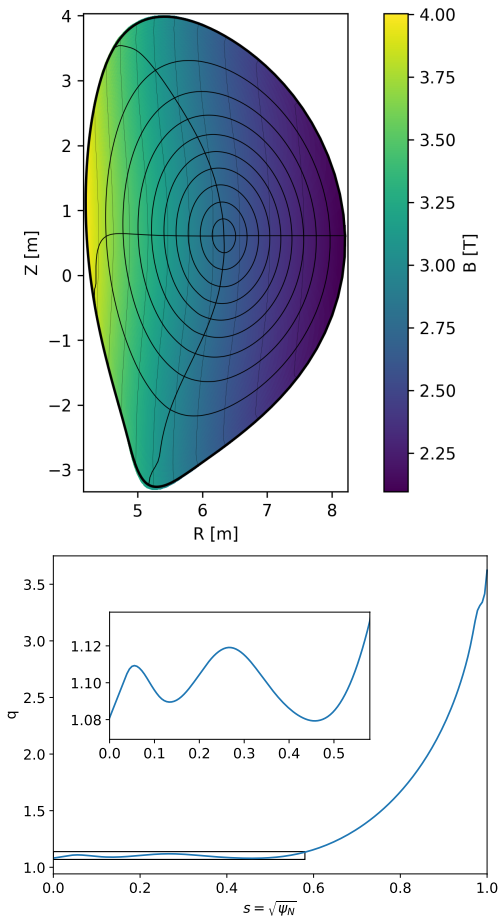


Figure 1: (a) ITER 15MA scenario equilibrium. The colour scale indicates  $|B|$ , the nested rings are surfaces of poloidal flux (equispaced in  $s = \sqrt{\Psi_N}$ ), the 4 lines which meet approximately at right angles in the centre are lines of constant straight-field-line poloidal angle ( $\theta^*$ ), the thin almost vertical lines are equispaced contours of  $|B|$ ; (b) the safety factor profile (with inset zoom showing the values in the inner part of the tokamak).

Due to the steep gradients at the edge of the plasma, we consider at most the region of the plasma  $0 \leq s \leq 0.9$ , which corresponds to the outermost interior ring plotted in figure 1(a).

Finally, while all simulations presented here are electromagnetic and performed with kinetic electrons, we increase the electron mass in order to reduce the numerical cost. In previous work [12], it was found that the mode damping was only weakly affected by increasing the electron mass, but that the numerical savings allowed more confidence in the numerical timestep convergence. Therefore, unless otherwise

but converges to its own solution. As a result, the  $q$ -profile obtained in the output of CHEASE is not identical to the  $q$ -profile from the IDS, as written by ASTRA.

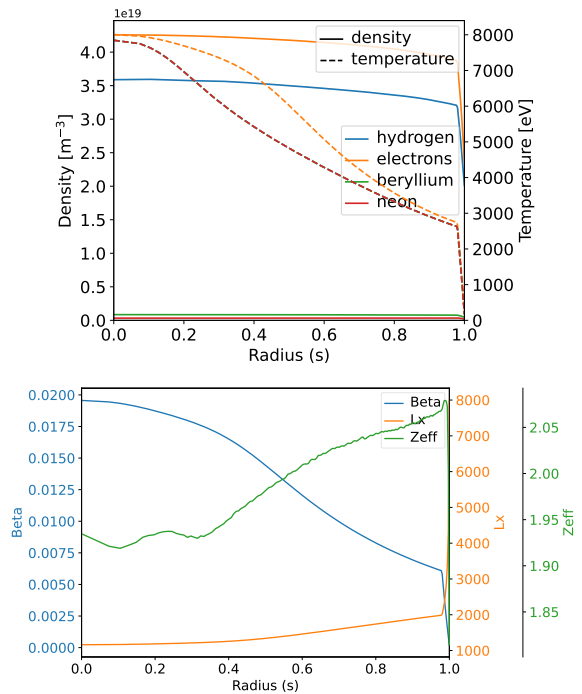


Figure 2: (a) Density (solid) and temperature (dashed) profiles for the bulk species in the scenario; (b) profiles of dimensionless quantities: electron  $\beta(s)$ ,  $L_x(s) = 2/\rho^*(s) = 2a/\rho_s(s)$ ,  $Z_{\text{eff}}(s)$ .

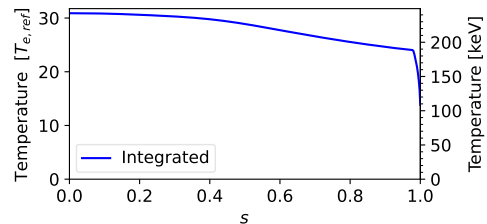


Figure 3: Energetic particle effective temperature profile, obtained by integrating the moments of the distribution function output from a simulation.

specified, the ratio of  $m_H/m_e$  shall be taken as 400.

## 4. Results

By changing the toroidal mode number(s) in the Fourier filter, it is possible to perform simulations of reduced systems, and thereby separate the physics scales of interest: of particular interest for linear studies. Unless stated otherwise, the simulations presented retain only a single toroidal mode number in the filter, and are initialized with a density perturbation (a perturbation on the particle weights depending only on the spatial coordinates) corresponding to the same toroidal mode number. The radial and poloidal structure of the

perturbation may vary, but is typically either radially broad and approximately field aligned (as is used in this work), or radially narrower, with e.g. a pair of poloidal harmonics designed to initialize the TAE, EAE, etc, in which case it will be radially located at the corresponding rational/half-rational surface of the TAE/EAE.

#### 4.1. Alfvén eigenmodes

We start by considering the range of Alfvén eigenmodes which might reasonably be expected to be driven unstable by the energetic particles, focussing on  $10 < n < 35$ .

First, we show  $n = 12$ , for which we perform a simulation with reduced mass ratio  $m_H/m_e = 400$ .

Running a simulation with  $N_p = (32, 128, 8, 8) \times 10^6$  markers for the hydrogen, electrons, beryllium, and neon species respectively. The simulation is performed with  $\Delta t = 10\omega_{ci}^{-1}$ , and  $\Delta m = 5$ , with a spatial grid resolution of  $(N_s, N_{\theta^*}, N_{\varphi}) = (1024, 192, 64)$ .

In figure 4, we show the poloidal cross section of the electrostatic potential at  $t = 40\,000\omega_{ci}^{-1}$ .

For the frequency evolution, we show in figure 6 how we fit the frequency, taking the example of  $s = 0.4685$  (the location of the peak in figure 5). In the upper panel, we plot the evolution of the envelope of the toroidal mode  $|\Phi_{n,s}(t)|$ . Fitting this from  $t > 20 \times 10^3 \omega_{ci}^{-1}$ , we obtain a growth rate of  $\gamma = -1.95 \times 10^{-3} \omega_A$ . We can now normalize the signal by multiplying  $\Re(\Phi_{n,s}(t))$  by  $e^{-\gamma t}$ . We then perform a Discrete Fourier transform of this normalized signal (again, for  $t > 20 \times 10^3 \omega_{ci}^{-1}$ ), the results of which are in the lower panel. In this case, we find  $(\omega, \gamma) = (0.222, -1.95 \times 10^{-3}) \omega_A$ , or  $f = 51.4$  kHz ( $\gamma/\omega = -0.88\%$ ). Such weak damping is sufficiently small that we might possibly expect these modes to be driven unstable when energetic particles are added [12].

If we perform the procedure described above on all radial points (independently), then we can stack the lower panels of figure 6 over radius, giving us a radial spectrogram, shown in figure 7. In this figure, we overlay the Alfvén continuum from LIGKA ¶ [13], both with and without the pressure upshift (BAE gap). This technique is designed to best identify frequencies, and we note that, since every radial position is normalized in a different way (to account for the growth/decay

¶ Taking the real part here is optional when dealing with a complex signal such as the toroidal/poloidal Fourier coefficients of the field. In such a case, we can refrain from taking the real part, and then the resulting analysis will allow us to differentiate between clockwise and anti-clockwise rotating modes. In cases where we analyse a real signal, however, the positive and negative frequency components in the output will necessarily be complex conjugates of each other, and the sign therefore has no meaning.  
¶ See discussion in Appendix A regarding differences in the safety factor profile used for ORB5 and LIGKA.

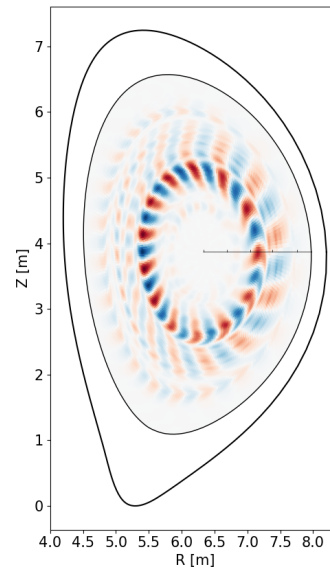


Figure 4: Poloidal cross section of the electrostatic potential for a simulation with  $n = 12$ .

of the signal), a direct comparison of different radial positions should not be attempted.

An alternative method to what we have described above, which can also isolate growth rates and frequencies from multiple components, is the DMUSIC algorithm [14], in which multiple complex frequencies are fit to the signal. However, where we have a single dominant component at a given radius, we appreciate the fast numerical speed and high intuitivity of the method that we have described.

Considering the analysis described here, we can say that the least damped modes for the  $n = 12$  case are a BAE/RSAE at  $s \approx 0.45$ ; and a TAE at  $s \approx 0.65$ . In addition, we also observe a weak EAE in the core, and another high frequency mode (high frequency RSAE or NAE (Triangularity-induced Alfvén eigenmode)), located around  $s = 0.15$  and  $s = 0.24$  respectively.

Next, we consider a simulation with  $n = 16$ . Similar to the analysis for  $n = 12$ , we show in figure 8 the radial profiles of the poloidal harmonics of the electrostatic potential  $\Phi$ . Here, we also mark with vertical lines the rational surfaces (solid) and half-rational surfaces (dashed). In figure 9, we again show the radial spectrogram of the analysis. Here we see some TAEs ( $s = (0.37, 0.52)$ ), with an RSAE at the minimum of  $q$  around  $s = 0.46$ . We also observe a very weak high frequency mode in the EAE gap at  $s \approx 0.25$ . Again, the observed damping is weak, with the measured fit damping rates  $-0.005 < \gamma/\omega_A \leq 0$  across a broad range of the plasma, in particular the region  $0.4 \leq s \leq 0.6$ .

Next we consider  $n = 20$ , for which we increase

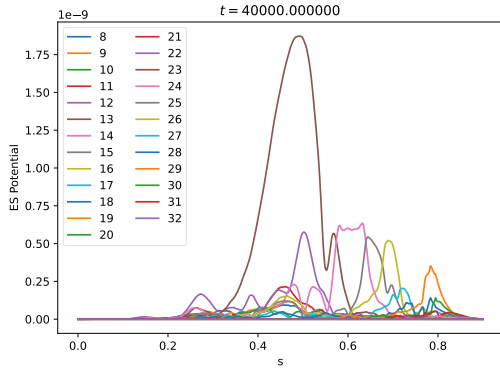


Figure 5: Plots of the absolute values of radial profiles of the  $(n, m) = (12, m)$  helicities of the electrostatic potential, with the legend corresponding to  $m$  (approximately increasing from core to edge with  $q(s)$ ).

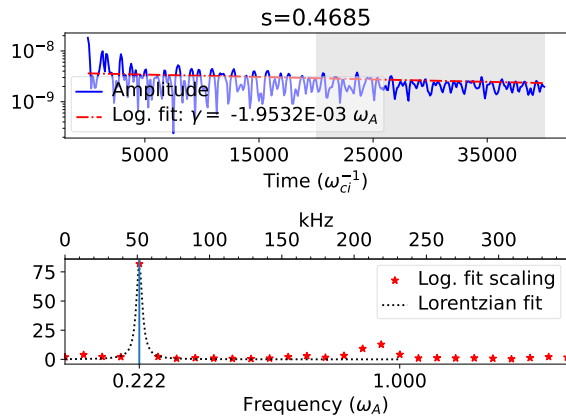


Figure 6: For the point  $s = 0.4685$ : (a) Plot of the  $n = 12$  envelope, with an exponential fit to the extrema in the range  $20000 < t\omega_{ci} < 40000$  (shaded grey). (b) Discrete Fourier transform of the electrostatic potential after dividing by the fitted exponential in (a).

$(N_s, N_{\theta^*}, N_{\varphi}) = (1024, 512, 128)$ . The radial profile of the electrostatic potential is shown in figure 10, showing a peak of two poloidal harmonics ( $m = 20$  and  $21$ ), peaked at approximately  $s = 0.45$ . We note that, even though this mode structure strongly reminds us of a TAE, we do not have a half-rational surface at  $s = 0.45$ , located between two rational surfaces ( $s = 0.350$ ,  $s = 0.537$ ), but not on a half-rational surface. We show in figure 12 that the minimum of the safety factor in this region is very close to the half-rational value of a TAE. From the spectrogram in figure 11, we note that the frequency of this mode is close to the bottom of the TAE gap, similar to behaviour also observed in the ramp-up phase of tokamaks [15, 16]. We therefore label this mode an TAE-like RSAE. We observe the

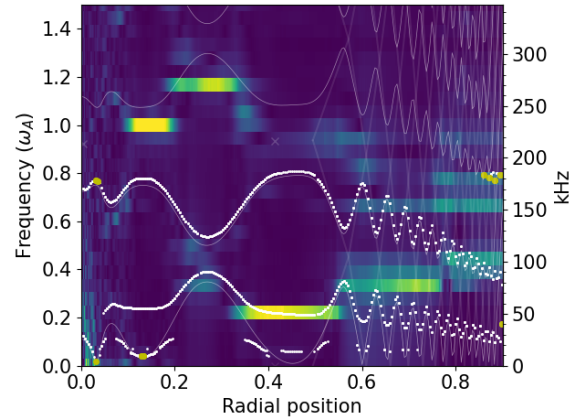


Figure 7: Radial frequency spectrogram for the electrostatic potential of the  $n = 12$  simulation,  $20000 < t\omega_{ci} < 40000$ . Some representations of the Alfvén continuum are overlotted. In thin white (curved) lines, the Alfvén continuum from the ideal kinetic model of LIGKA (neglecting pressure effects). In thick white dots, the continuum from the kinetic model of LIGKA, with the points being shown in large yellow dots if the imaginary part of the continuum  $\Im(\omega) > 0$ . In thin (straight) white lines ( $s > 0.5$ ) and crosses, a simple model (implemented directly in the ORB5 diagnostics) for the continuum, with crossing points marking the analytical location of AEs.

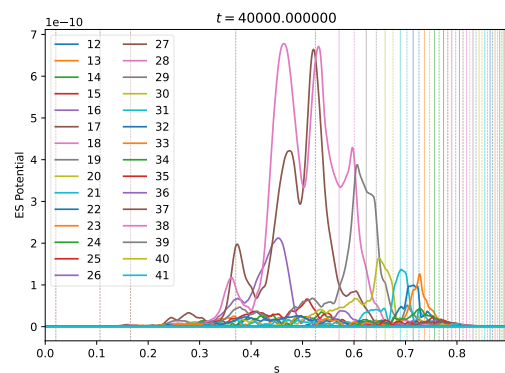


Figure 8: Plots of the absolute values of radial profiles of the  $(n, m) = (16, m)$  helicities of the electrostatic potential, with the legend corresponding to  $m$ . Solid vertical lines of a given colour correspond to the location(s) of the  $q = m/n$  rational surface associated with the  $m$  in the legend; dashed vertical lines to the half-rational surfaces  $q = (m + \frac{1}{2})/n$ .



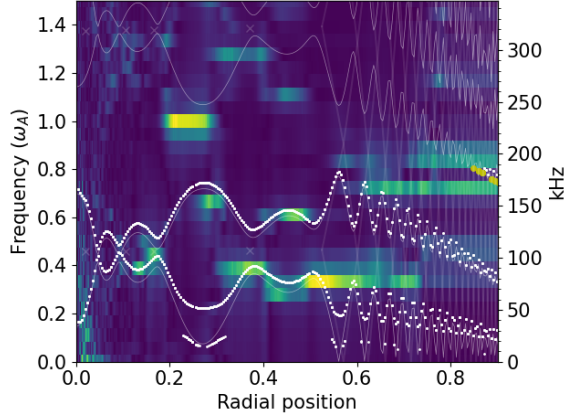


Figure 9: Radial frequency spectrogram for electrostatic potential of the  $n = 16$  simulation,  $20000 < t\omega_{ci} < 40000$ . For the explanation of the overplotted Alfvén continuum, see figure 7.

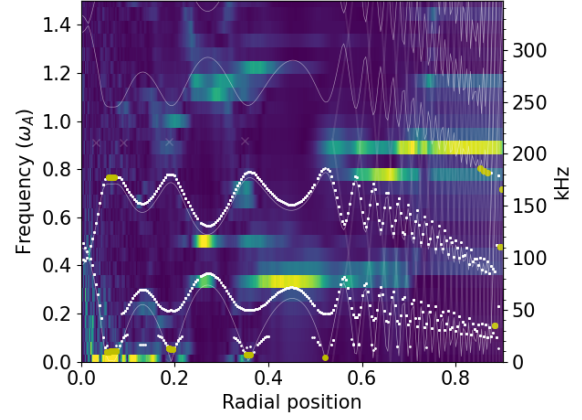


Figure 11: Radial frequency spectrogram for electrostatic potential of the  $n = 20$  simulation,  $20000 < t\omega_{ci} < 40000$ . For the explanation of the overplotted Alfvén continuum, see figure 7.

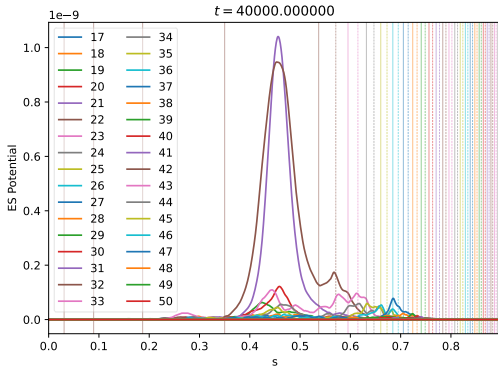


Figure 10: Plots of the absolute values of radial profiles of the  $(n, m) = (20, m)$  helicities of the electrostatic potential, with the legend corresponding to  $m$ .

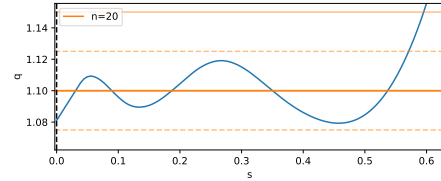


Figure 12: Safety factor profile in core of the plasma with the  $n = 20$  rational (solid) and the half-rational (dashed) surfaces marked.

weakest growth in the region  $0.3 \leq s \leq 0.5$ , where  $|\gamma| < 0.005\omega_A$ , where the damping is weak and the mode is close to marginal stability.

For  $n = 24$ , from figures 13 and 14, we find the predominant modes are found in the EAE band, distributed between  $s = 0.4$  and  $0.6$ .

For  $n = 32$ , like the case of  $n = 20$ , we see a narrow TAE-like mode structure in figure 15, with the dominant poloidal harmonics  $m = (34, 35)$ . Once again in the frequency, we see that the mode is in the gap of the minimum of the safety profile, with a frequency close to the TAE frequency. Since  $(21 + \frac{1}{2})/20$  and  $(34 + \frac{1}{2})/32$  are very similar, 1.075 and 1.078125 respectively, we can compare to figure 12, and apply the same arguments regarding the proximity of  $q_{TAE}$  and the  $q_{min}$ .

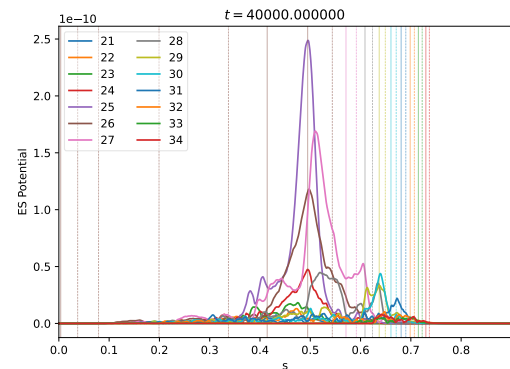


Figure 13: Plots of the absolute values of radial profiles of the  $(n, m) = (24, m)$  helicities of the electrostatic potential, with the legend corresponding to  $m$ . Since the number of poloidal harmonics in the simulation is large ( $21 \leq m \leq 59$ ), we show only  $m \leq n + 10$ .

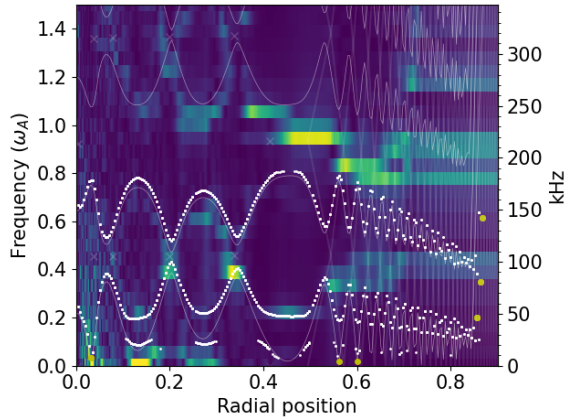


Figure 14: Radial frequency spectrogram for electrostatic potential of the  $n = 24$  simulation,  $20000 < t\omega_{ci} < 40000$ . For the explanation of the overplotted Alfvén continuum, see figure 7.

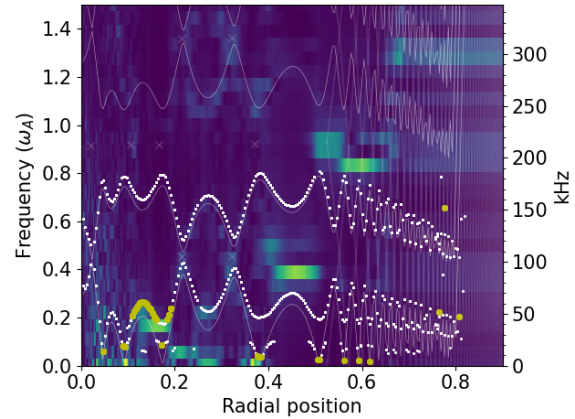


Figure 16: Radial frequency spectrogram for electrostatic potential of the  $n = 32$  simulation,  $20000 < t\omega_{ci} < 40000$ . For the explanation of the overplotted Alfvén continuum, see figure 7.

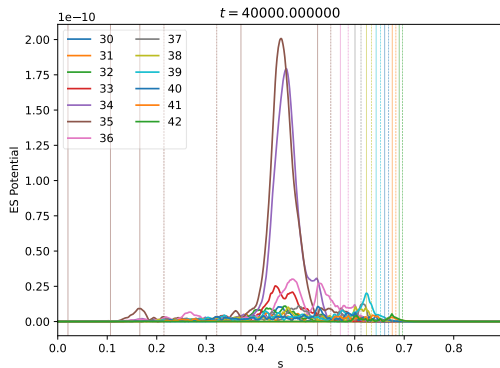


Figure 15: Plots of the absolute values of radial profiles of the  $(n, m) = (32, m)$  helicities of the electrostatic potential, with the legend corresponding to  $m$ . Since the number of poloidal harmonics in the simulation is large ( $30 \leq m \leq 77$ ), we show only  $m \leq n + 10$ .

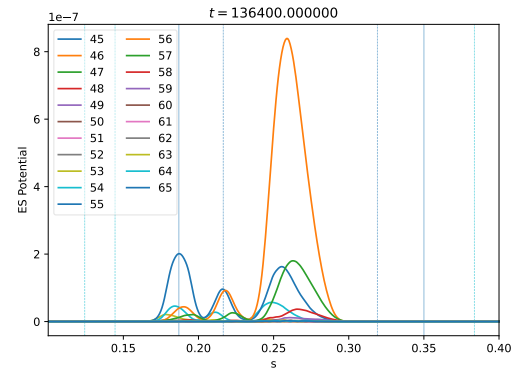


Figure 17: Plots of the absolute values of radial profiles of the  $(n, m) = (50, m)$  helicities of the electrostatic potential, with the legend corresponding to  $m$ . Vertical lines correspond to the locations of rational and half-rational surfaces, see figure 8.

#### 4.2. Unstable mesoscale modes

Further increasing the toroidal mode number, we observe a transition to a very localized instability close to the  $q_{\max}$  at  $s = 0.27$ . We therefore present analysis for simulations performed on a reduced radial domain,  $0.1 \leq s \leq 0.4$ , which retain the physical effects, but allows us to reduce the numerical cost for such simulations (both in terms of reducing the required radial resolution as well as the  $q_{\max}$ , and therefore the poloidal resolution required to resolve  $m \approx nq_{\max}$ . We therefore run a simulation for  $n = 50$  with,  $(N_s, N_{\theta^*}, N_{\varphi}) = (384, 480, 240)$ . This simulation has been performed with the number of markers,  $N_p = (64, 64, 16, 16) \times 10^6$ , for H,  $e^-$ , Be, Ne.

In figure 17, we can see that the dominant mode is single poloidal harmonic ( $m = 56$ ) peaked at  $s = 0.26$ .

We also see a secondary peak of  $m = 55$  peaked at the rational surface at  $s = 0.187$ . In figure 18, we see that the mode is growing with a clearly identified growth rate and frequency,  $(\omega, \gamma) = (0.1658, 6.7 \times 10^{-3}) \omega_A$ , or  $f = 38.4$  kHz ( $\gamma/\omega = 4.0\%$ ).

If we extend this case to include other toroidal mode numbers, we find that after a fixed amount of time, the electrostatic potential on outboard midplane can be visualized in figure 19. Here we see a pattern with a near periodicity of  $\Delta n$  of approximately 8. We can understand this pattern by noting that the local  $q_{\max} = 1.1191$ , and therefore the proximity of the rational surfaces to the  $q_{\max}$  is periodic with  $1/(1 - q_{\max}) = 8.4$ . This also explains why a peak in intensity is observed for  $n = 59$ , since the rational fraction  $66/59$  is the closest approximation of  $q_{\max}$  in



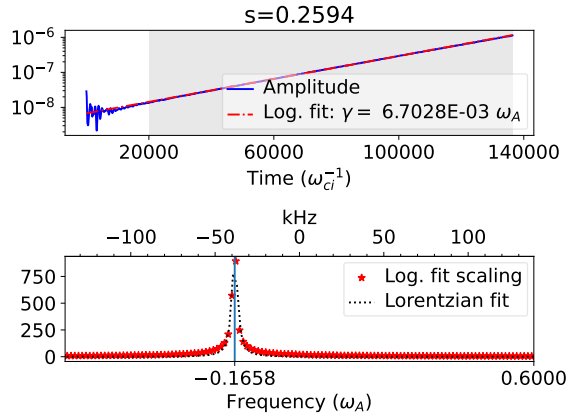


Figure 18: For the point  $s = 0.259$ : (a) Plot of the  $n = 50$  envelope, with an exponential fit to the extrema in the range  $20000 < t\omega_{ci}$  (shaded grey). (b) Discrete Fourier transform of the electrostatic potential after dividing by the fitted exponential in (a).

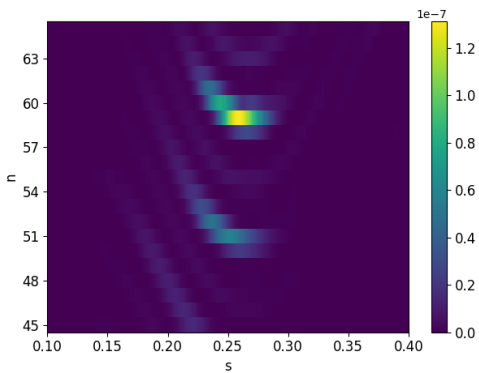


Figure 19: Snapshots of the electrostatic potential on the outboard midplane for 21 simulations with  $n = \{45, \dots, 65\}$  at  $t\omega_{ci} = 40000$ , plotted against the radius and the toroidal mode number.

this range of  $n$  in the denominator.

In figure 20, we show the frequency and growth rate for these cases, both located at the  $q_{\max}$  (a), and at the location of the mode peak (b). Here we can further see the almost periodic behaviour in the growth and frequency.

Regarding the mode drive, we show in figure 21 the spectrogram, but we draw particular attention to the kinetic spectrum overplotted from LIGKA. This is obtained from the local kinetic model of LIGKA, and we have plotted in yellow the points where the imaginary part of the continuum frequency is positive. Since the mode that we observe corresponds with tip of this unstable continuum, and since the mode is close to the position where the  $q_{\max}$  is close to the value of a rational fraction, we label this mode

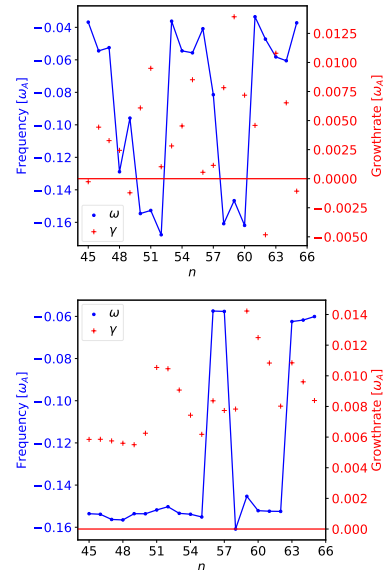


Figure 20: Frequency (blue lines) and growth rate (red points) for different mode numbers fit at the radial position of (a) the maximum of  $q$  at  $s = 0.265$ , (b) the location of the respective peak instability.

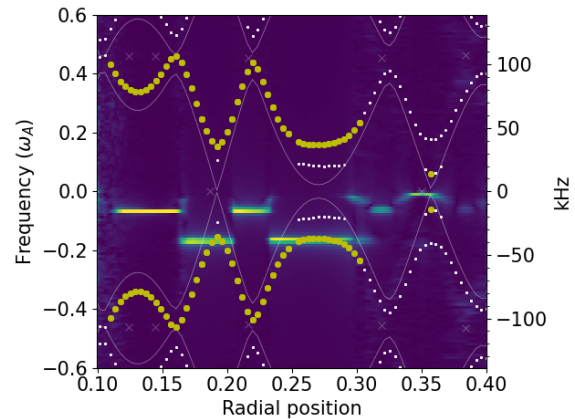


Figure 21: Radial frequency spectrogram for electrostatic potential of the  $n = 50$  simulation,  $20000 < t\omega_{ci}$ . For the explanation of the overplotted Alfvén continuum, see figure 7. The Fourier analysis has been performed on the complex spatial Fourier coefficients, and therefore the sign of the frequency can be determined. In this case, the LIGKA data has been mirrored in the  $\Im(\omega) = 0$  plane.

a BAE [17], or Alfvénic Ion Temperature Gradient (AITG) mode [18, 19], although we note that the mode also has similarities with the RSAE. We find  $(\omega, \gamma) = (-0.152, 6.15 \times 10^{-3}) \omega_A$ .

Wanting to be sure that the artificial electron mass is not responsible for the mode growth in the simulations, we perform also a simulation with

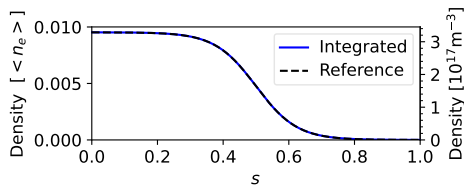


Figure 22: Energetic particle density profile, obtained by integrating the moments of the distribution function output from a simulation.

$m_H/m_e = 1600$  (close to nominal). We therefore reduce the time step to  $\Delta t = 1.5 \omega_{ci}^{-1}$ , and obtain values of  $(\omega, \gamma) = (-0.169, 7.93 \times 10^{-3}) \omega_A$ .

Further decreasing the time step to  $\Delta t = 0.5 \omega_{ci}^{-1}$ , we find  $(\omega, \gamma) = (-0.161, 8.91 \times 10^{-3}) \omega_A$ , or  $f = -37.4$  kHz ( $\gamma/|\omega| = 5.5\%$ ). We therefore have confidence that this mode is driven unstable by the bulk plasma in the model considered, and not that this is a numerical instability. For a detailed discussion of the effect of the electron mass and the time step on the numerical convergence, we refer to Reference [12].

**4.2.1. Effect of energetic particles on BAE/AITG modes** An interesting question is whether energetic particles might have any effect on such a mode such as this bulk-plasma-driven mode. Still with the  $m_H/m_e$  and  $\Delta t = 0.5 \omega_{ci}^{-1}$ , we therefore add a simplified population of NBI particles, using an isotropic slowing down distribution with an injection energy of 1 MeV. The effective temperature of this distribution depends weakly on radius and is shown in figure 3. We consider a simplified density profile for the NBI, shown in figure 22, constructed with a *tanh* function.

With the addition of the NBI, we find  $(\omega, \gamma) = (-0.164, 8.88 \times 10^{-3}) \omega_A$ , or  $f = -38.1$  kHz ( $\gamma/|\omega| = 5.4\%$ ).

We therefore state that energetic particles, at least those considered here, have no effect on the linear behaviour of these BAE/AITG modes.

### 4.3. Microscale instabilities

Considering now the microscales, we perform a study of large toroidal mode numbers, looking for ion gyroradius-scale micro-instabilities (such as those associated with turbulence).

We consider the radial domain  $0.4 \leq n \leq 0.7$ , the region with the steepest electron temperature gradient and consider toroidal mode numbers in the range  $n > 120$ , increasing the toroidal resolution to keep  $N_\varphi > 3n$ , ideally  $\geq 4n$ , but also choosing convenient values for parallelization.

We begin below by showing the case of  $n = 180$ , with  $(N_s, N_{\theta^*}, N_\varphi) = (384, 1152, 576)$ . In the late

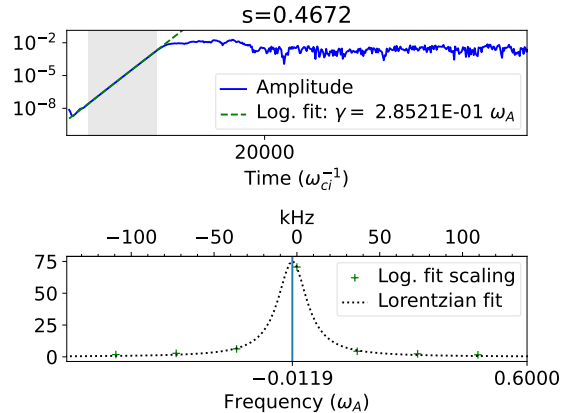


Figure 23: For the point  $s = 0.4672$ : (a) Plot of the  $n = 180$  envelope, with an exponential fit to the extrema in the range  $2000 < t\omega_{ci} < 9000$  (shaded grey). (b) Discrete Fourier transform of the electrostatic potential after dividing by the fitted exponential in (a).

linear phase, we find a peak at  $s = 0.467$ , from where we measure low or zero frequency, and a growth rate of  $\gamma = 4.15 \times 10^5 \text{ s}^{-1}$ .

In the case of a larger mode number,  $n = 216$ , we find that the mode is linearly stable. For a smaller mode number,  $n = 160$ , we find a much weaker growth rate, which allows us to measure more accurately the linear (non-zero) frequency, finding ( $5000 \leq t\omega_{ci}^{-1} \leq 54300$ )  $\omega = -4.7$  kHz,  $\gamma = 5.9432 \times 10^4 \text{ s}^{-1}$ .

We have therefore identified this range of toroidal mode numbers,  $n < 216$ , with a peak of  $\gamma$  for  $n \approx 180$ , which driven unstable by bulk-plasma gradients.

## 5. Summary and outlook

In conclusion, we have shown a multi-scale nature of instabilities in this ITER PFPO scenario. By means of global electromagnetic gyrokinetic simulations with ORB5, we have identified three classes of eigenmode/instability, namely the weakly damped ‘macroscale’ Alfvén eigenmodes in the range  $n = [10 \rightarrow 35]$ , a range of ‘mesoscale’ unstable bulk-plasma driven Alfvénic instabilities in the range  $n = [45 \rightarrow 60]$ , and a range of unstable ‘microscale’ instabilities in the range  $n = [150 \rightarrow 220]$ .

We have shown that, for an isotropic slowing down distribution function of NBI energetic particles with  $E_{\text{birth}} = 1$  MeV, the growth rates of these mesoscale modes appear insensitive to the addition of energetic particles, although a more realistic treatment of the EP distribution function is left for future work.

We have identified a number of effects (that we refer to as ‘multi-scale’) which would be of strong interest to consider in a unified setting. Since

there are partially different radial locations key to the different single-scale phenomena, the nonlinear interplay of these different scales would be interesting. Considering the numerical demands of dealing with large mode numbers, and time scale separation and radial domains, this would be very demanding, however we think that we have laid out the scales and phenomena which such an effort should retain.

Finally, we note that the label ‘macroscale’ is often used to refer to MHD instabilities, for example fishbone and sawtooth physics, which are not included in this study, but are also relevant for this scenario. We note that the safety factor profile,  $q(s)$ , is of major importance for the Alfvénic modes, and any sawtooth activity will lead to a change in this profile. It is therefore of particular interest to consider time-dependent scenarios, which should especially be considered with reduced models [20]. The study of these MHD phenomena (in isolation) is of interest from (gyro-)kinetic codes or (kinetic-) MHD models, especially since these might lead to a redistribution of the energetic particle profile.

## Acknowledgements

The authors would like to acknowledge A. Polevoi for providing the scenario data through IMAS, and to S. Pinches and M. Schneider for discussions relating to the scenario and to dealing with IMAS data. The authors would like to acknowledge discussions with those participating in the ITPA-EP activity B.11.12, and the associated collaboration with the ISEP SciDAC project. The authors would also like to thank the members of the ORB5 team. This work has been carried out within the framework of the EUROfusion Consortium, funded by the European Union via the Euratom Research and Training Programme (Grant Agreement No 101052200 – EUROfusion). Views and opinions expressed are however those of the author(s) only and do not necessarily reflect those of the European Union or the European Commission. Neither the European Union nor the European Commission can be held responsible for them. Simulations presented in this work were performed on the MARCONI FUSION HPC system at CINECA and the HPC systems of the Max Planck Computing and Data Facility (MPCDF).

## Appendix A. Comparison of safety factor profile

As noted previously, when we overlay the Alfvén continuum from LIGKA, we must note that the safety factor profile is not consistent between LIGKA and ORB5, since these two codes interface to different

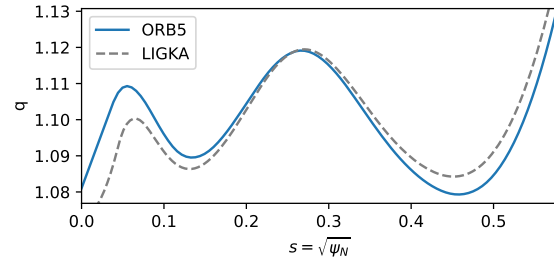


Figure A1: Comparison of the safety factor profiles (ORB5, from CHEASE; LIGKA, from HELENA) in the core of the plasma. The ‘ORB5’ line corresponds to the inset plot in figure 1(b).

equilibrium solvers, HELENA [21] and CHEASE respectively. Since these equilibrium solvers have different boundary conditions at the magnetic axis, there is not an exact match of the  $q$ -profile. We have taken care to match the  $q$ -profile as closely as possible in the core region, especially to match the region relevant for §4.2. We therefore plot a comparison of the safety factor profiles in figure A1.

## References

- [1] E. Lanti, N. Ohana, N. Tronko, T. Hayward-Schneider, A. Bottino, B. F. McMillan, A. Mishchenko, A. Scheinberg, A. Biancalani, P. Angelino, S. Brunner, J. Dominiski, P. Donnel, C. Gheller, R. Hatzky, A. Jocksch, S. Jolliet, Z. X. Lu, J. P. Martin Collar, I. Novikau, E. Sonnendrücker, T. Vernay, and L. Villard. ORB5: a global electromagnetic gyrokinetic code using the PIC approach in toroidal geometry. *Computer Physics Communications*, 251, 2020.
- [2] A. Mishchenko, A. Bottino, A. Biancalani, R. Hatzky, T. Hayward-Schneider, N. Ohana, E. Lanti, S. Brunner, L. Villard, M. Borchardt, R. Kleiber, and A. Könies. Pullback scheme implementation in ORB5. *Computer Physics Communications*, 238, 2019.
- [3] Ph. Lauber, S. Günter, A. Könies, and S.D. Pinches. LIGKA: A linear gyrokinetic code for the description of background kinetic and fast particle effects on the MHD stability in tokamaks. *Journal of Computational Physics*, 226(1), 2007.
- [4] B.F. McMillan, S. Jolliet, A. Bottino, P. Angelino, T.M. Tran, and L. Villard. Rapid Fourier space solution of linear partial integro-differential equations in toroidal magnetic confinement geometries. *Computer Physics Communications*, 181, 2010.
- [5] A.R. Polevoi, A. Loarte, R. Bilato, N. Gorelenkov, Ye.O. Kazakov, E. Polunovskiy, A. Tchistiakov, E. Fable, V. Kiptily, A.V. Krasilnikov, A.Y. Kuyanov, R. Nazikian, S.D. Pinches, and M. Schneider. Impact of suprathermal ions on neutron yield in the pre-DT phase of ITER operation. *Nuclear Fusion*, 61(7):076008, 2021.
- [6] A. Loarte, A.R. Polevoi, M. Schneider, S.D. Pinches, E. Fable, E. Militello Asp, Y. Baranov, F. Casson, G. Corrigan, L. Garzotti, D. Harting, P. Knight, F. Koechl, V. Parail, D. Farina, L. Figini, H. Nordman, P. Strand, and R. Sartori. H-mode plasmas in the pre-

- fusion power operation 1 phase of the ITER research plan. *Nuclear Fusion*, 61(7):076012, 2021.
- [7] G.V. Pereverzev and P.N.Yushmanov. ASTRA automated system for transport analysis in a tokamak. *Max-Planck IPP Report*, 5(98), 1991.
- [8] F. Imbeaux, S.D. Pinches, J.B. Lister, Y. Buravand, T. Casper, B. Duval, B. Guillerminet, M. Hosokawa, W. Houlberg, P. Huynh, S.H. Kim, G. Manduchi, M. Owsiak, B. Palak, M. Plociennik, G. Rouault, O. Sauter, and P. Strand. Design and first applications of the ITER integrated modelling & analysis suite. *Nuclear Fusion*, 55(12):123006, 2015.
- [9] F. Vannini, A. Biancalani, A. Bottino, T. Hayward-Schneider, P. Lauber, A. Mishchenko, E. Poli, B. Rettino, G. Vlad, X. Wang, and the ASDEX Upgrade team. Gyrokinetic modelling of the Alfvén mode activity in ASDEX Upgrade with an isotropic slowing-down fast-particle distribution. *Nuclear Fusion (sub.)*, 2022.
- [10] B. Rettino, T. Hayward-Schneider, A. Biancalani, A. Bottino, Ph. Lauber, I. Chavdarovski, F. Vannini, and F. Jenko. Gyrokinetic modelling of anisotropic energetic particle driven instabilities in tokamak plasmas. *Nuclear Fusion (sub.)*, 2022.
- [11] H. Lütjens, A. Bondeson, and O. Sauter. The CHEASE code for toroidal MHD equilibria. *Computer Physics Communications*, 97, 1996.
- [12] T. Hayward-Schneider, Ph. Lauber, A. Bottino, and Z.X. Lu. Global linear and nonlinear gyrokinetic modelling of Alfvén eigenmodes in ITER. *Nuclear Fusion*, 61:036045, 2021.
- [13] Ph. Lauber, M. Brüdgam, D. Curran, V. Igochine, K. Sassenberg, S. Günter, M. Maraschek, M. García-Muñoz, N. Hicks, and the ASDEX Upgrade Team. Kinetic Alfvén eigenmodes at ASDEX Upgrade. *Plasma Physics and Controlled Fusion*, 51(12), 2009.
- [14] R. Kleiber, M. Borchardt, A. Könies, and C. Slaby. Modern methods of signal processing applied to gyrokinetic simulations. *Plasma Physics and Controlled Fusion*, 63(3):035017, 2021.
- [15] Ph. Lauber. Super-thermal particles in hot plasmas – kinetic models, numerical solution strategies, and comparison to tokamak experiments. *Physics Reports*, 533(2), 2013.
- [16] M.A. Van Zeeland, W.W. Heidbrink, S.E. Sharapov, D. Spong, A. Cappa, Xi Chen, C. Collins, M. García-Muñoz, N.N. Gorelenkov, G.J. Kramer, P. Lauber, Z. Lin, and C. Petty. Electron cyclotron heating can drastically alter reversed shear alfvén eigenmode activity in DIII-d through finite pressure effects. *Nuclear Fusion*, 56(11):112007, 2016.
- [17] W. W. Heidbrink. Basic physics of Alfvén instabilities driven by energetic particles in toroidally confined plasmas. *Physics of Plasmas*, 15(5), 2008.
- [18] Fulvio Zonca, Liu Chen, and Robert A Santoro. Kinetic theory of low-frequency alfvén modes in tokamaks. *Plasma Physics and Controlled Fusion*, 38(11), 1996.
- [19] Fulvio Zonca, Liu Chen, Robert A Santoro, and J Q Dong. Existence of discrete modes in an unstable shear alfvén continuous spectrum. *Plasma Physics and Controlled Fusion*, 40(12), 1998.
- [20] V.-A. Popa. Workflow-based energetic particle stability analysis of projected ITER plasmas. M.Sc. thesis, Technische Universität München, 2021.
- [21] G.T.A. Huysmans, J.P. Goedbloed, and W. Kerner. Isoparametric bicubic Hermite elements for solution of the Grad-Shafranov equation. *Proc. CP90 Conf. on Comp. Phys. Proc.*, page 371, 1991.